Periodic attractors in two-photon processes

Paul Mandel and N. P. Pettiaux
Université Libre de Bruxelles, Campus Plaine, Code Postal 231, B-1050 Bruxelles, Belgium

Wang Kaige,* P. Galatola, and L. A. Lugiato
Dipartimento di Fisica, Politecnico di Torino, 10129 Torino, Italy
(Received 30 July 1990)

We consider three nonlinear optical models that display a two-photon process and exhibit a Hopf bifurcation corresponding to a phase instability. The three models describe second-harmonic generation, two-photon optical bistability, and degenerate four-wave mixing in resonant cavities. In all three cases we consider only the resonant configuration and analyze the attractors which emerge when the driving field is increased beyond the Hopf bifurcation threshold. At a finite distance from threshold, we find a hysteresis domain that involves a pair of periodic attractors. For all three models, each of the two solutions has the same "field portrait" i.e., the same representation in a plane whose axes are the imaginary and the real parts of the electric field. This suggests that the scenario is generic for this class of systems. On the other hand, the models for two-photon optical bistability and degenerate four-wave mixing in resonant cavities exhibit additional nongeneric attractors when the driving field is further increased.

I. INTRODUCTION

The modeling of optical nonlinear processes in resonant passive cavities leads to a set of complex ordinary differential equations for the electric fields and, possibly, for the atomic variables in the semiclassical description. It is often useful to have a guiding principle for the classification of the solutions of these equations. This has been made especially clear in studies of chaotic solutions for which a classification is applied both to the approach to the strange attractor (the so-called scenarios) as well as the nature of chaos itself. The relevance of these classification schemes lies in the assumption that a given type of behavior can be linked to a broad class of equations and therefore of nonlinearities. In other terms, there should be a correspondence between the elementary physical processes whose description generates the nonlinear equations and the nature of the solutions. Quite often, however, it is the converse approach which takes place first, namely, the phenomenological observation that a class of physical processes leads to a class of temporal solutions (spatial variations related to transverse effects will not be considered here). In a recent paper[1] it has been shown that two-photon processes in a resonant electromagnetic cavity driven by a coherent cw input beam share instability properties of the steady states. In particular these authors proved that (i) there is almost always a Hopf bifurcation that leads to periodic solutions and (ii) in resonance, this instability can be ascribed exclusively either to the phases or to the amplitudes of the fields. The purpose of the present paper is to elaborate on this analysis by considering the nature of the periodic attractors occurring beyond the Hopf bifurcation point when the instability is due only to the phase of the fields. In Ref. 1, three models were analyzed that belong to this category: second-harmonic generation (SHG), two-photon optical bistability (2OB) and degenerate four-wave mixing (DFWM). We shall analyze these three models sequentially in order of increasing complexity, beginning with SHG and finishing with DFWM. The main feature which we shall show is that at a finite distance from the Hopf bifurcation, a hysteresis domain appears which involves a pair of stable periodic attractors (i.e., optical bistability for periodic solutions). In this connection, a problem that arises is how to characterize these different periodic attractors. The usual procedure is to compare the time series of the periodic solutions, in particular for the intensities. This information is readily available theoretically when analytical solutions are known, numerically by direct integration of the differential equations and experimentally by recording photon numbers. However this approach neglects the complex nature of the electric field whose phase is precisely the dynamical variable which drives the system out of its stable steady state. As shown recently[2] it is possible (though by no means simple) to measure simultaneously the field amplitude and phase. We have found that a useful representation for our purposes is the field portrait, i.e., a representation of the solution in a plare whose coordinates are the real and the imaginary parts of the field, also known as the quadrature components. Our result is that in this plane, each of the two periodic solutions which overlap in the hysteresis has the same field portrait for all three models, the portrait of the two coexisting solutions being unmistakingly different. Our analysis suggests that the presence and the behavior of these two attractors is generic for the systems which display two-photon processes and exhibit a Hopf bifurcation associated with a phase instability. It must be said, however, that each system in this class may present, in

addition to these attractors, further attractors which are nongeneric. For lack of an adequate method to investigate analytically these models well beyond the Hopf bifurcation, our results will be basically numerical with a few analytic results whenever possible. In Sec. II, we study SHG. In Sec. III we consider 2OB while in Sec. IV we present an analysis of DFWM.

II. SECOND-HARMONIC GENERATION

The prototype of the three models we shall study is the second harmonic generation in a resonant passive cavity[3] which is described by the pair of equations

$$\gamma_1^{-1}\frac{dA_1}{dt}=-A_1-A_1^*A_2+E_1\ ,$$
$$\gamma_2^{-1}\frac{dA_2}{dt}=-A_2+A_1^2\ , \tag{2.1}$$

where A_j are the complex electric fields inside the cavity, E_1 is the coherent input field, and γ_j are the cavity field damping rates. To derive these equations, it has been assumed that the input field and A_1 have frequency ω_1 while A_2 has frequency $\omega_2=2\omega_1$ and that the two frequencies ω_1 and ω_2 coincide with cavity resonances. The arbitrary phase of the input field E_1 is chosen to be zero. For the type of analysis we shall perform, a new scaling of the time and the fields is useful to further reduce the number of relevant parameters. We define the new variables

$$R_1(\tau)=(\gamma_1/\gamma_2)^{1/2}A_1(t),\ R_2(\tau)=-(\gamma_1/\gamma_2)A_2(t)\ ,$$
$$E=(\gamma_1/\gamma_2)^{3/2}E_1\ , \tag{2.2}$$
$$\tau=\gamma_2 t,\quad \gamma=\gamma_1/\gamma_2\ ,$$

in terms of which the dynamical equations take the form

$$R_1'=-\gamma R_1+R_1^*R_2+E\ ,$$
$$R_2'=-R_2-R_1^2\ , \tag{2.3}$$

where $R'\equiv dR/d\tau$. As shown by Drummond, McNeil, and Walls[3] this system of equations has a steady-state solution which becomes unstable via a Hopf bifurcation. The emerging solution was studied for the general case $\gamma\neq 0$ in Ref. 4 and the particular case $\gamma=0$ was analyzed with a simpler method in Ref. 5. Since there was an algebraic mistake in the calculation of Ref. 4, we shall summarize the main analytical results here. In steady state, R_1 and R_2 are real functions. The field R_1 is the unique real solution of

$$R_1^3+\gamma R_1-E=0\ , \tag{2.4}$$

and R_2 is given by $R_2=-R_1^2$. This steady-state solution is stable for $E<E_H$ with the scaled input field at the bifurcation point being defined as:

$$E_H=(1+2\gamma)\sqrt{1+\gamma}\ . \tag{2.5}$$

When $E=E_H$, the two fields become

$$R_{1,H}=\sqrt{1+\gamma},\quad R_{2,H}=-(1+\gamma)\ . \tag{2.6}$$

At the Hopf bifurcation, spontaneous oscillations arise with a frequency

$$\Omega_H^2=1+2\gamma\ . \tag{2.7}$$

The extension of the single time approach used in Ref. 5 to the case $\gamma\neq 0$ leads to the following results. In the vicinity of the instability threshold, the periodic solutions can be expanded in a power series as

$$R_1(\tau)=R_{1,H}+i\varepsilon(e^{iT}+e^{-iT})+O(\varepsilon^2)\ ,$$
$$R_2(\tau)=R_{2,H}+i\varepsilon\left[\frac{-1+i\sqrt{1+2\gamma}}{\sqrt{1+\gamma}}e^{iT}-\frac{1+i\sqrt{1+2\gamma}}{\sqrt{1+\gamma}}e^{-iT}\right]+O(\varepsilon^2)\ , \tag{2.8}$$

where $0<\varepsilon\ll 1$ is defined through $E=E_H+\varepsilon^2E_2$ while $T=[1+\varepsilon^2\omega_2+O(\varepsilon^3)]\Omega_H\tau$. A direct calculation of ω_2 and E_2 using the solvability condition leads to

$$\omega_2=\frac{9(1+2\gamma)(3+2\gamma)}{17+8\gamma(3+2\gamma)^2}\ ,$$
$$E_2=\frac{(1+2\gamma)[99+4\gamma(73+56\gamma+16\gamma^2)]}{2\sqrt{1+\gamma}[17+8\gamma(3+2\gamma)^2]}\ . \tag{2.9}$$

The positivity of E_2 implies the stability of the emerging periodic solution and the supercriticality of the Hopf bifurcation.

As already noticed in Ref. 4, at a finite distance from the Hopf bifurcation there is a domain in which two stable periodic solutions have overlapping domains of existence. We have now investigated this domain of hysteresis in more detail. Using the software AUTO (Ref. 6) we have been able to follow the stable and unstable solutions of the scaled Eqs. (2.3), thereby giving evidence of a real S-shaped curve. In Fig. 1 we have plotted the

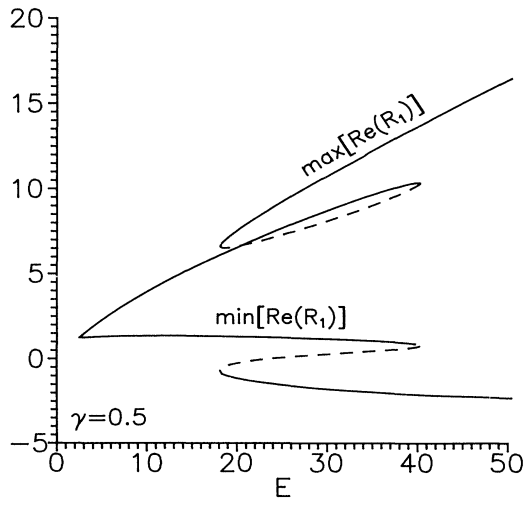

FIG. 1. The minimum and the maximum amplitudes of the periodic solutions emerging at the Hopf bifurcation $E_H=1$ in SHG. Solid lines correspond to stable periodic solutions, dashed lines to unstable periodic solutions.

minimum and the maximum values of the periodic amplitudes for $\gamma=\frac{1}{2}$ and for a range of the control parameter E that fully includes the bistable domain. Similarly in Fig. 2 we have reported the frequency of the periodic solutions (normalized to the Hopf frequency $\Omega_H=\sqrt{1+2\gamma}$) for the same range of E. To avoid confusion, let us emphasize at this point that we shall call the lower branch the branch of solutions which emerges from the Hopf bifurcation at $E=E_H=(1+2\gamma)\sqrt{1+\gamma}$. The best way we found to distinguish the lower and upper branch solutions is to construct their field portraits. This is done in Fig. 3, which displays the "figure eight" field portrait corresponding to the lower branch solutions and the "butterfly," which corresponds to the upper branch solutions. One property which has always been verified is that in the case of the "figure eight" field portrait, the real part of the field never becomes negative while for the "butterfly" field portrait the real part has always a positive and a negative part, so that the time behavior of the intensity $|R_1|^2$ might erroneously suggest a period-doubling phenomenon.[7] Along the unstable branch, there is a continuous deformation of the figure eight into a butterfly as shown in Fig. 4 for $\gamma=\frac{1}{2}$. It should be noted that a purely harmonic solution has an figure eight field portrait. Thus this portrait is associated with the solution which has the lowest content of harmonics of the fundamental frequency in its spectrum. This appears clearly if we consider the time series associated with these two phase portraits (see Refs. 5 and 12 where these time series are displayed for SHG and 2OB, respectively). Next we have tried to characterize the width of the hysteresis domain as a function of the only remaining parameter γ. This was done purely numerically and led to the results reported in Fig. 5. In these figures E_- and Ω_- refer to the properties of the upper branch limit point while E_+ and Ω_+ refer to the lower branch limit point. We have plotted $E_\pm$ for selected values of γ in the interval $0\le\gamma\le1$. The solid lines which connect the points are fitting curves. For $E_\pm$ their equations are

$$E_+=39.41\gamma^4+23.30\gamma^3+46.12\gamma^2+30.65\gamma+8.09\ , \tag{2.10}$$

$$E_-=6.52\gamma^2+18.99\gamma+6.96\ . \tag{2.11}$$

Since these are fitting curves, there is a large amount of arbitrariness in the type of curve chosen, as we have no analytic result that can restrict our choice. However, the divergence of E_- in γ^2 can be verified quite simply by analyzing the asymptotic limit $\gamma\to\infty$. To study the domain $\gamma>1$, it is more adequate to introduce the scaling

$$S_1(T)=\gamma' R_1(t),\quad S_2(T)=-\gamma' R_2(t),\quad \bar{E}=(\gamma')^2E\ ,\quad T=\gamma\tau,\quad \gamma'=\gamma_2/\gamma_1=1/\gamma\ , \tag{2.12}$$

which leads to

$$S_1'=-S_1+S_1^*S_2+\bar{E}\ ,\qquad S_2'=-\gamma' S_2-S_1^2\ , \tag{2.13}$$

where $S'\equiv dS/dT$. In fact, the results which were obtained in Ref. 1 refer explicitly to the limit $\gamma'\to0$. In that limit it is quite simple to verify numerically that there still remains a hysteresis with a limit point $\bar{E}_-$ at a finite distance from the origin for $\gamma'=0$. From this fact it follows that

$$\bar{E}_-(\gamma'=0)=\gamma^{-2}E_-(\gamma=\infty)=\text{finite constant}\ , \tag{2.14}$$

which implies that $E_-(\gamma)$ must diverge like γ^2. However, the series expansion in integer powers of γ is only an assumption. On the other hand, the result (2.10) for E_+ implies that $\bar{E}_+(\gamma'=0)$ should be infinite. All we can report is that we have been unable to locate $\bar{E}_+$ for small values of γ'. A similar analysis for the frequency of the periodic solutions at the boundaries of the hysteresis domain has been performed and is displayed in Fig. 5(b). The two fitting curves are

$$\Omega_+=0.50\gamma^3+0.39\gamma^2+0.77\gamma+0.35\ , \tag{2.15}$$

$$\Omega_-=0.2456\gamma+0.2763\ . \tag{2.16}$$

Here again there is a certain measure of arbitrariness in

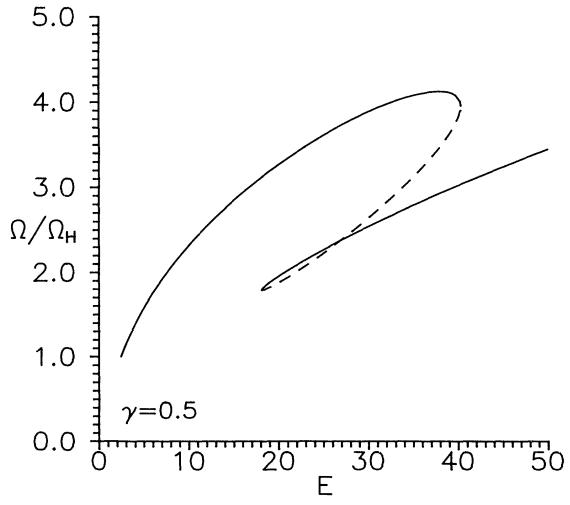

FIG. 2. Frequency of the periodic solution described in Fig. 1 in units of the frequency at the bifurcation.

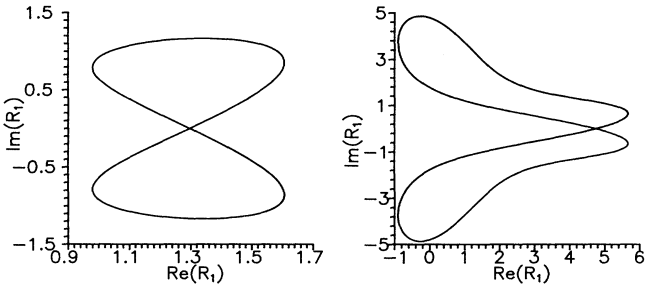

FIG. 3. Field portraits of the two stable periodic solutions of Fig. 1 for $E=20$ and $\gamma=\frac{1}{2}$.

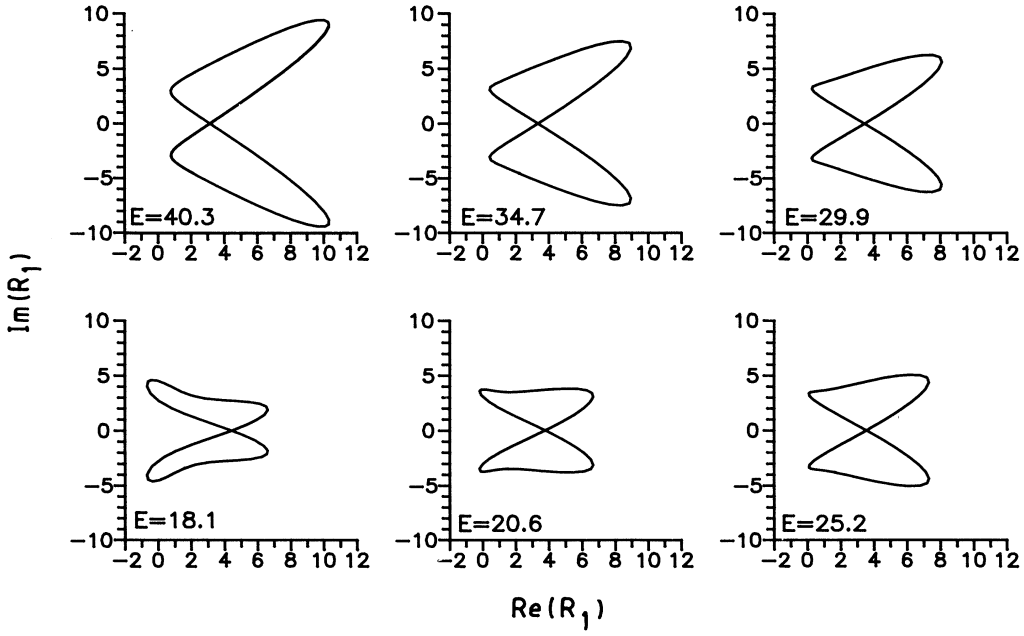

FIG. 4. Field portraits of the periodic solution along the unstable branch of Fig. 1. Note that all six figures have the same axes.

the choice of the fitting curves. However the scaling argument which leads to the result (2.14) also applies to the frequency and gives the result

$$\gamma^{-1}\Omega_{-}(\gamma=\infty)=\text{finite constant}\ , \tag{2.17}$$

which indeed agrees with Eq. (2.16).

III. TWO-PHOTON OPTICAL BISTABILITY

The next model that we analyze is the two-photon optical bistability[8] (2OB). This model has been extensively studied in relation with the generation of squeezed states.[9–12] Periodic solutions emerging from a phase instability were also reported[7] but the fact that the two types of periodic solutions have a hysteresis domain escaped the attention of these authors. The coupled equations for the field x, the atomic polarization v, and the population difference m under resonance conditions are

$$\begin{aligned}\kappa^{-1}\frac{dx}{dt}&=-x+y-2Cx^{*}v\ ,\\ \gamma_{\perp}^{-1}\frac{dv}{dt}&=-v+x^{2}m\ ,\\ \gamma_{\parallel}^{-1}\frac{dm}{dt}&=-\tfrac{1}{2}[(x^{*})^{2}v+x^{2}v^{*}]-m+1\ ,\end{aligned} \tag{3.1}$$

where y is the real positive input field, C the bistability parameter, and κ, $\gamma_{\perp}$, and $\gamma_{\parallel}$ are the decay rates of the cavity field, the polarization, and the population difference, respectively. All variables have been suitably scaled. Although these equations do not bear any resemblance to the equations governing SHG, an asymptotic

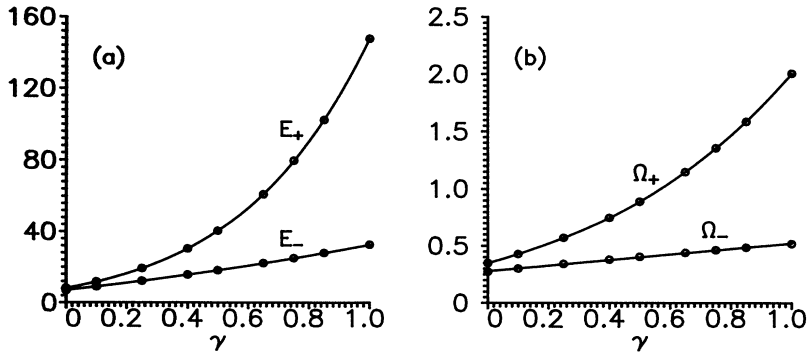

FIG. 5. Properties of the limit points defining the bistable domain of the periodic solutions vs γ. (a) Maximum (E_{+}) and minimum (E_{-}) of the input field defining the width of the hysteresis domain. (b) Frequency at the limit points. The dots are the results of direct numerical integrations. The connecting lines are fitting curves.

analysis reveals that such a connection does indeed exist. Let us define a new set of variables and parameters via

$$R_1=(2\kappa C/\gamma_\perp)^{1/2}x,\quad R_2=-(2\kappa C/\gamma_\perp)v\ ,$$
$$E=\frac{\kappa}{\gamma_\perp}(2\kappa C/\gamma_\perp)^{1/2}y\ , \tag{3.2}$$
$$\gamma=\kappa/\gamma_\perp,\quad f=\gamma_\parallel/(2\gamma_\perp),\quad \tau=\gamma_\perp t\ .$$

In terms of these new functions, Eqs. (3.1) become

$$R_1'=-\gamma R_1+R_1^*R_2+E\ ,$$
$$R_2'=-R_2-R_1^2m\ , \tag{3.3}$$
$$m'=2f(1-m)+\frac{f}{4\gamma^2C^2}[(R_1^*)^2R_2+R_1^2R_2^*]\ .$$

In the long-time limit and for $\gamma C\to\infty$, the population difference becomes $m=1+O(1/\gamma^2C^2)$ and the remaining equations for R_1 and R_2 are asymptotically identical to the SHG equations analyzed in Sec. II.

The steady-state solutions of Eqs. (3.1) are the real solutions of

$$y=x\left[1+\frac{2Cx^2}{1+x^4}\right]\ .$$

The solution $x=x(y,C)$ has a domain of bistability for $C\geq 2.71$. The linear stability of this steady solution indicates that the negative slope branch of the bistable domain is always unstable. Furthermore, when $C\geq 1+\gamma^{-1}$, the steady solution is unstable in the domain[7]

$$x_-<x<x_+\ , \tag{3.4}$$

with

$$x_\pm=[\bar{C}\pm(\bar{C}^2-1)^{1/2}]^{1/2},\quad \bar{C}=C\gamma/(1+\gamma)\ .$$

The instabilities at $x_\pm$ are Hopf bifurcations due to the phases. With the normalization (3.2) the unstable domain can be equivalently characterized by the condition

$$E/R_1>1+2\gamma\ , \tag{3.5}$$

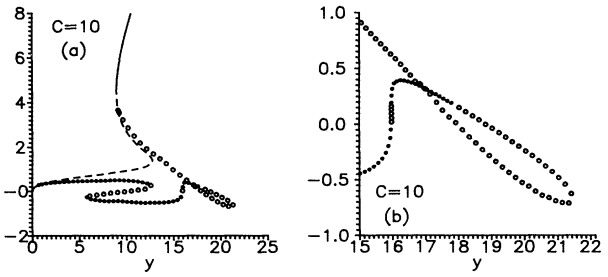

FIG. 6. Bifurcation diagram for 2OB with $\gamma=2$, $f=1$, and $C=10$. The solid lines represent stable steady states, the dashed line represents unstable steady states, the black dots represent stable periodic solutions and open dots represent unstable periodic solutions. For the periodic solutions, we have displayed only the minimum of the field amplitudes X.

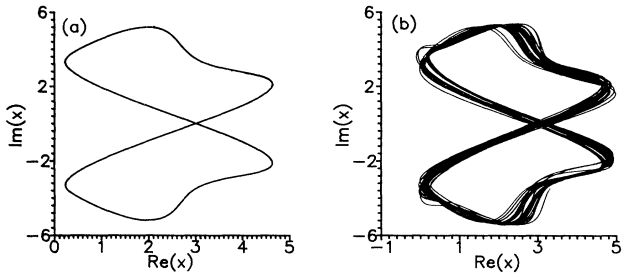

FIG. 7. Field portraits for 2OB with $\gamma=2$, $f=1$, and $C=10$. (a) $y=17.5$; stable periodic solution. (b) $y=18.1$: chaotic solution.

which coincides with the instability domain in SHG [see Eqs. (2.5) and (2.6)]. The Hopf frequency also coincides with that of SHG, given by Eq. (2.7). On the other hand, the existence of two Hopf bifurcation points and the increased number of parameters with respect to SHG leads to a richer bifurcation diagram. In Fig. 6 we have displayed a typical bifurcation diagram for $f=1$, $\gamma=2$, and $C=10$. For the sake of legibility, we have only reported on the graphs the minimum of the periodic solutions. Furthermore, Fig. 6(b) displays an enlargement of a critical portion of Fig. 6(a). In Fig. 6(a) we see that a branch of periodic solutions emerges from the first Hopf bifurcation. On this branch, the periodic solution is stable and corresponds to one of the branches of the hysteresis loop which we expect to observe. This is indeed the case and a well-developed bistable domain for the periodic solutions can be seen. However a third nongeneric branch of solutions is also present. It looses its stability away from a limit point, i.e., via a secondary bifurcation. The continuation of this branch remains unstable and connects to the second Hopf bifurcation of the steady state. A direct numerical integration of Eqs. (3.1) indicates that beyond the secondary bifurcation point of the third periodic branch a period-doubling cascade leads to chaos. The field portrait of the third stable branch of periodic solutions and of the emerging chaotic solution is shown in Fig. 7.

IV. DEGENERATE FOUR-WAVE MIXING

The third model that we analyze in this paper is DFWM, which under resonance conditions can be described by the following set of equations for the two complex fields A_1 and A_2[13]:

$$\gamma_1^{-1}\frac{dA_1}{dt}=-A_1-A_1^*A_2^2+\bar{E}\ ,$$
$$\gamma_2^{-1}\frac{dA_2}{dt}=-A_2-A_1^2A_2^*\ , \tag{4.1}$$

with damping rates γ_j for the mode j and real pump field amplitude $\bar{E}$. For $0\leq\bar{E}<1$, the unique steady-state solution of Eqs. (3.1) is

$$A_1=\bar{E}\ ,$$
$$A_2=0\ . \tag{4.2}$$

This trivial solution becomes unstable for $\bar{E}>1$: at $\bar{E}=1$, the steady state bifurcates to the new stable stationary solution

$$A_1=1\ ,\qquad A_2=\pm(\bar{E}-1)^{1/2}\ . \tag{4.3}$$

Again this nontrivial solution loses its stability via a Hopf bifurcation for

$$\bar{E}>2\left[1+\frac{\gamma_2}{\gamma_1}\right]\ . \tag{4.4}$$

Similar to what we showed for 2OB, in this case also it is possible to establish an asymptotic connection with SHG. Let us consider the transformation equations

$$R_1=A_1,\quad R_2=-\frac{\gamma_1}{2\gamma_2}A_2^2\ ,\qquad E=\frac{\gamma_1}{2\gamma_2}\bar{E},\quad \tau=2\gamma_2 t,\quad \gamma=\frac{\gamma_1}{2\gamma_2}\ . \tag{4.5}$$

They lead to the new field equations:

$$R_1'=-\gamma R_1+R_1^* R_2+E\ ,\qquad R_2'=-R_2-|R_2|R_1^2\ . \tag{4.6}$$

Here again, the SHG equations (2.3) are not exactly recovered, but as long as R_2 is an $O(1)$ function, the equations should display qualitatively the same type of solutions as in SHG: as a matter of fact, with the help of Eqs. (4.3) and (4.5), the instability condition can be cast in the same general form (3.5) and also normalized Hopf frequency coincides with Eq. (2.7).

A major difference between Eqs. (4.1) and the equations describing SHG and 2OB are the symmetry properties of (4.1). Indeed, if $\mathbf{A}=(A_1, A_2)$ is a solution of (4.1), then the following pairs are also solutions of the same equations:

$$\mathbf{A}^*=(A_1^*, A_2^*),\quad \mathbf{B}=(A_1,-A_2),\quad \mathbf{B}^*=(A_1^*,-A_2^*)\ . \tag{4.7}$$

The transition from $\mathbf{A}$ to $\mathbf{A}^*$ is obtained by performing a rotation of π of the phase plane around the real axis, for both modes A_1 and A_2, whereas the transition from $\mathbf{A}$ to $\mathbf{B}^*$ is achieved by a rotation of π around the real axis for mode A_1 and around the imaginary axis for mode A_2. Clearly, the transformation that leads from $\mathbf{A}$ to $\mathbf{B}^*$ is the product of two transformations $\mathbf{A}\rightarrow\mathbf{A}^*$ and $\mathbf{A}\rightarrow\mathbf{B}$, in whatever order.

In SHG and 2OB, the existence of solution $\mathbf{A}$ implies only that $\mathbf{A}^*$ is also a solution. The two additional solutions $\mathbf{B}$ and $\mathbf{B}^*$ are typical of DFWM; the origin is especially transparent in the notation of Eqs. (4.6). Furthermore, the four solutions $\mathbf{A}$, $\mathbf{A}^*$, $\mathbf{B}$, and $\mathbf{B}^*$ are all associated with the same partial intensities or photon numbers $I_j=|A_j|^2$.

The presence of additional solutions $\mathbf{B}$ and $\mathbf{B}^*$ arises from the fact that the DFWM model has analogies not only with SHG, but also with the degenerate parametric oscillator.[3] As a matter of fact, all solutions (4.7) exist also in that system; the analogy between DFWM and degenerate parametric oscillator has been exploited in Ref. 13.

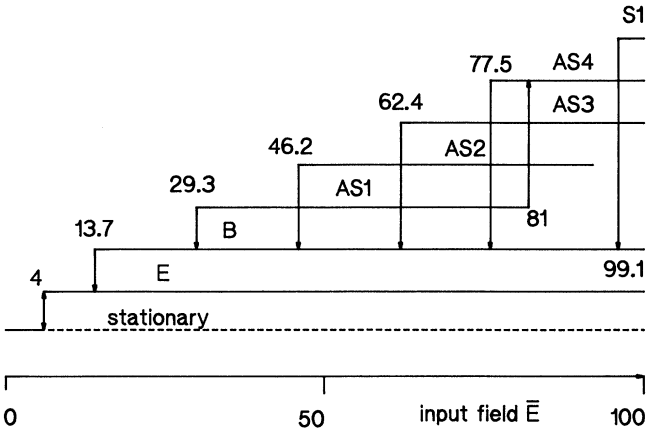

FIG. 8. Schematic representation of the domains of existence and the transitions among the various solutions in DFWM for $\gamma_1=\gamma_2$ as a function of the normalized filed $\bar{E}$.

Even though the DFWM equations are characterized by the same number of parameters as the SHG equations, the bifurcation diagram for DFWM displays a much larger complexity, because several periodic solutions can coexist. Fig. 8 schematically represents the situation that one encounters for increasing values of the input field $\bar{E}$ with the fixed ratio $\gamma_1/\gamma_2=1$. The solutions labeled E and B correspond to the figure eight and butterfly field trajectories, respectively, in accordance with the general scheme already met in the previous two models. The four solutions labeled AS1 to AS4 correspond, instead, to periodic solutions that are asymmetrical with respect to the transposition $A\rightarrow A^*$. The solutions ASn ($n=1,\ldots,4$) display a similar shape, but the number of intensity pulses over each period of the intensity increases with n. Figure 9 illustrates the field portraits of the pump [Fig. 9(a)] and of the signal [Fig. 9(b)] mode for the simplest solution of this family, AS1, for $\bar{E}=29$ and $\gamma_1=\gamma_2$. The signal mode is characterized by four main "legs" forming angles of 90°; each leg has in turn a fine structure of three legs leading to a total of 12 legs. On the other hand, the pump mode is characterized by three main legs split, respectively, in one, two, and three legs, leading to a total of six legs. The period T_1 of the pump mode is one-half the period T_2 of the signal mode, so that in a complete period T_2 of the system, the number of intensity pulses of the pump and of the signal modes is equal. We note also that due to the symmetry of the phase plane pattern with respect to the transformation $A\rightarrow B$, the period of the *intensity* of the signal mode is $T_2/2$. Table I summarizes the main features of the asymmetric solutions for the pump and the signal modes: the total number of legs in the field portrait, the number of legs in each

TABLE I. Schematic outline of the principal characteristics of the asymmetrical solutions ASn ($n=1,2,3,4$) in DFWM.

	Total legs in one period	Number of legs in each quadrant 1	2	3	4	Visiting sequence of the quadrants in one period	T_2/T_1
				Pump mode A_1			
AS1	6	2	0	1	3	$(1\to4)^2\to3\to4$	
AS2	10	3	0	2	5	$(1\to4\to3\to4)^2\to1\to4$	
AS3	14	4	0	3	7	$(1\to4\to3\to4)^3\to1\to4$	
AS4	18	5	0	4	9	$(1\to4\to3\to4)^4\to1\to4$	
				Signal mode A_2			
AS1	12	3	3	3	3	$(1\to4)^3\to(3\to2)^3$	2
AS2	10	2	3	3	2	$(1\to4)^2\to(3\to2)^3$	1
AS3	28	7	7	7	7	$(1\to4)^3\to(3\to2)^2\to(1\to4)^2\to(3\to2)^3\to(1\to4)^2\to(3\to2)^2$	2
AS4	18	4	5	5	4	$(1\to4)^2\to(3\to2)^2\to(1\to4)^2\to(3\to2)^3$	1

of the four quadrants of the phase plane (the quadrants are numbered sequentially counterclockwise starting from the top right quadrant), the sequence according to which the different quadrants are visited as time flows [the notation $(i\to j\cdots)^n$ means that the sequence $i\to j\cdots$ is repeated n times], and the ratio between the period T_2 of the signal mode and the period T_1 of the pump mode. The periods of the intensities of the two modes are always equal and are also equal to the period T_1 of the pump mode. By inspection of the table, one easily sees that the number of intensity pulses of the two modes over each complete period of the system (which is already equal to the period T_2 of signal mode) is equal. Increasing the input field $\bar{E}$ above 99.1, one meets anoth-

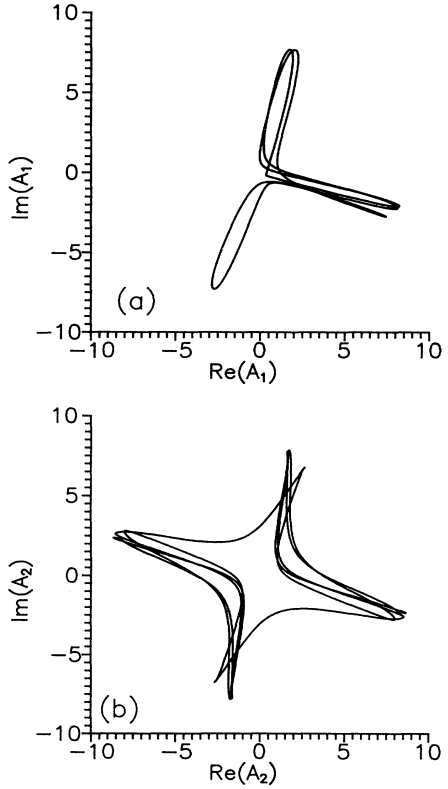

FIG. 9. Field portraits of (a) the pump and (b) the signal modes in DFWM for $\bar{E}=29.1$, $\gamma_1=\gamma_2$ corresponding to the AS1 solution.

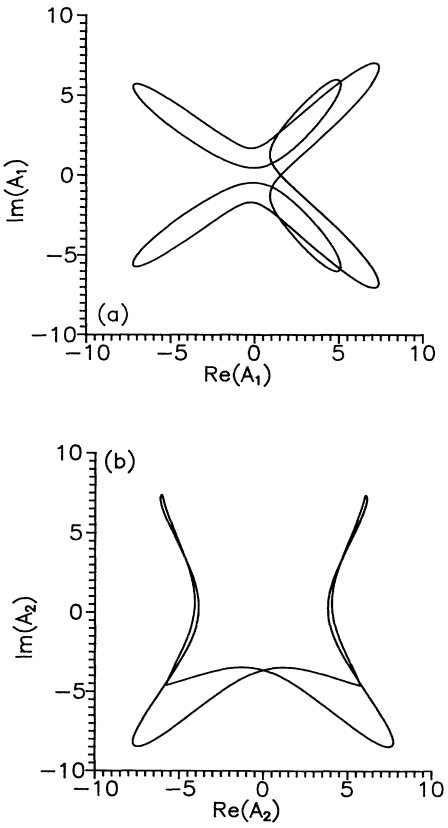

FIG. 10. Same as Fig. 9 but for $\bar{E}=99.2$: the "S1" solution.

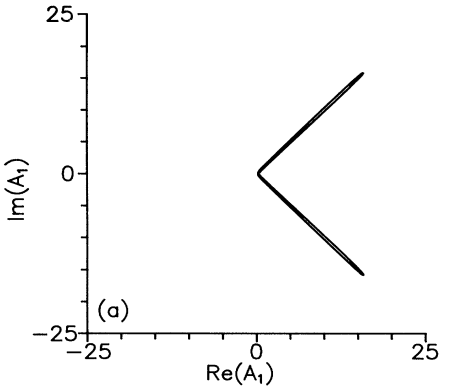

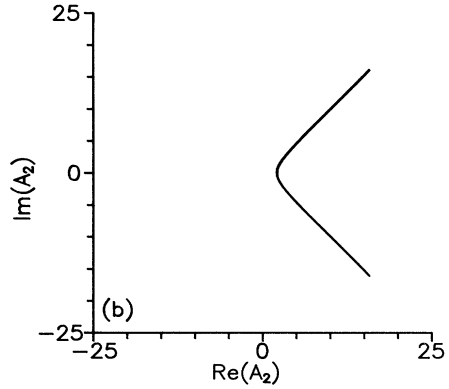

FIG. 11. The figure eight in DFWM for $\bar{E}=70$: (a) pump mode, (b) signal mode.

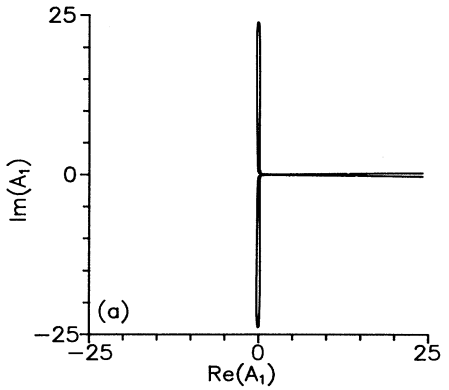

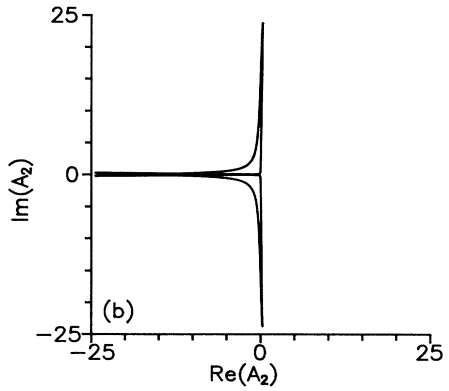

FIG. 12. Same as Fig. 11 but for the butterfly.

er kind of periodic solution, which we call S1, completely different from the asymmetric solutions ASn ($n=1,\ldots,4$). Its field portrait is shown in Fig. 10(a) for the pump mode and Fig. 10b for the signal model. The S1 pattern is symmetrical with respect to the transformation $A\rightarrow B^*$; the number of intensity pulses over each period of the intensity is 3 for both modes, as a consequence of this symmetry. The attractors ASn ($n=1,\ldots,4$) and S1 are nongeneric.

For values of $\bar{E}$ larger than 100, it becomes increasingly difficult, from a numerical viewpoint, to follow the different solutions, which tend to acquire more and more stretched shapes. For instance in Figs. 11 and 12, we show the field portraits corresponding to the figure eight and the butterfly for $\bar{E}=70$: the spikes become very narrow and eventually look like single straight lines.

For this reason, we have not been able to find the value (which presumably exists) of the upper limit point E_+ where the figure eight solution becomes unstable, and where the system would perform a transition to the butterfly. On the other hand, if we start from a solution of the type ASn ($n=1,\ldots,4$) or S1 and decrease gradually $\bar{E}$, this solution becomes unstable below a certain value of $\bar{E}$, and the system performs a transition to the butterfly pattern (see Fig. 8). The butterfly solution becomes in turn unstable at the lower limit point $\bar{E}=13.7$. Finally we note that for $\bar{E}=93.1$, the periodic solution AS2 does not jump to another periodic solution but becomes chaotic.

For DFWM, we have concentrated our attention to the sequence of attractors which are connected to the figure eight and the butterfly. This, however, does not include all possible attractors since, e.g., a large-amplitude limit cycle can be found to coexist with the steady-state solution at $\bar{E}=2$.

ACKNOWLEDGMENTS

P.M. and N.P.P. are supported by the Fonds National de la Recherche Scientifique (Belgium) and the Interuniversity Attraction Pole of the Belgian government. W.K. is supported by the International Centre for Theoretical Physics Programme for Training and Research in Italian Laboratories (Trieste). This research was also supported in part by the Italian Ministry for University Scientific and Technological Development and by the ESPRIT Basic Research Action NOROS (Quantum Noise Reduction in Optical Systems).

*On leave of absence from the Department of Physics of Beijing Normal University, Beijing, People's Republic of China.

[1]L. A. Lugiato, P. Galatola, and L. M. Narducci, Opt. Commun. **76**, 276 (1990).

[2]H. Zeghlache, P. Mandel, N. B. Abraham, and C. O. Weiss, Phys. Rev. A **38**, 3128 (1988); C. O. Weiss, N. B. Abraham, and U. Hübbner, Phys. Rev. Lett. **61**, 1587 (1988).

[3]P. D. Drummond, K. J. McNeil, and D. F. Walls, Opt. Acta **27**, 321 (1980); **28**, 211 (1981).

[4]P. Mandel and T. Erneux, Opt. Acta **29**, 7 (1982).

[5]P. Mandel and T. Erneux, in *Laser Physics,* Vol. 182 of *Lecture Notes in Physics,* edited by J. D. Harvey and D. F. Walls (Springer, Heidelberg, 1983), p. 132.

[6]E. J. Doedel, Cong. Num. **30**, 265 (1981).

[7]P. Galatola, L. A. Lugiato, M. Vadacchino, and N. B. Abraham, Opt. Commun. **69**, 414 (1989).

[8]F. T. Arecchi and A. Politi, Lett. Nuovo Cimento **23**, 65 (1978).

[9]L. A. Lugiato and G. Strini, Opt. Commun. **41**, 374 (1982).

[10]C. M. Savage and D. F. Walls, Phys. Rev. A **33**, 3282 (1986).

[11]B. A. Capron, D. A. Holm, and M. Sargent III, Phys. Rev. A **35**, 3388 (1987).

[12]P. Galatola, L. A. Lugiato, M. Vadacchino, and N. B. Abraham, Opt. Commun. **69**, 419 (1989).

[13]C. M. Savage and D. F. Walls, J. Opt. Soc. Am. B **4**, 1514 (1987).